CHEMISTRY OF MATERIALS

pubs.acs.org/cm Article

Above-Room-Temperature $LiNbO_3$-Type Polar Magnet Stabilized by Chemical and Physical Pressure

Yifeng Han, Chuanhui Zhu, Yi Peng, Shufang Li, MeiXia Wu, Shuang Zhao, Zheng Deng, Changqing Jin, Wei Du, David Walker, and Man-Rong Li*

Cite This: *Chem. Mater.* 2020, 32, 1618−1626 Read Online

ACCESS | Metrics & More | Article Recommendations | Supporting Information

ABSTRACT: $LiNbO_3$ (LN)-type polar magnets are technologically important but require stringent and costly high-pressure synthesis with very limited sample yields. We develop a chemical strategy to reduce the physical synthesis pressure. LN-type polar magnets require 7 GPa to stabilize in the high-pressure Mn_2FeNbO_6 (MFNO) phase. Here, MFNO was successfully stabilized in the isostructural LN matrix at intermediate physical pressure (below 5 GPa) at gram levels for each run by dilution with LN according to $(Li_{1-x}Mn_x)(Fe_{x/2}Nb_{1-x/2})O_3$ (x = 0.18, 0.33, 0.46, 0.57). LN-diluted MFNO demonstrates ferromagnetism above room-temperature (magnetic ordering temperature $T_C \approx 516-554$ K) and has large estimated spontaneous polarization ($P_S \approx 18-63\ \mu C/cm^2$). Irreversible c-axis near-zero thermal expansion stemming from magnetostriction was observed around the magnetic transition temperature region upon heating at ambient pressure, which irreversibly elongates the distance between the face-sharing (Li/Mn) and (Fe/Nb) octahedral centroids along the c-axis and thus weakens the magnetic interactions. The magnetic ordering temperature drops in the annealed samples. The findings in $(Li_{1-x}Mn_x)(Fe_{x/2}Nb_{1-x/2})O_3$ show that polar magnets can be made by chemical pressure together with soft physical pressure and shed light on large-scale and lower cost stabilization of high-pressure phases.

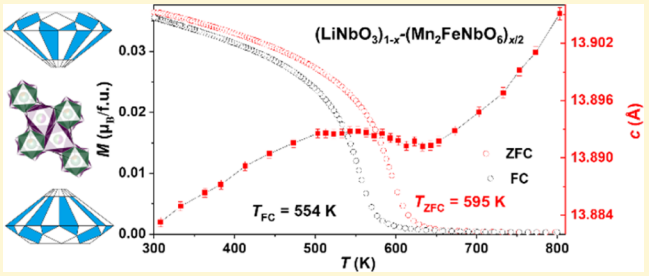

1. INTRODUCTION

$LiNbO_3$ (LN)-type materials demonstrate properties originating from their polar nature,[1−4] including ferroelectricity, second harmonic generation (SHG), and multiferroicity. Examples include $ATiO_3$ (A = Fe,[1] Mn,[2,4] Zn[5]), $ASnO_3$ (A = Mn,[4] Zn[3]), and Mn_2FeMO_6 (M = Nb and Ta, disordered B/B′; M = Mo and W, ordered B/B′).[6−11] However, most of the exotic, perovskite-related LN-type compounds require high-pressure and temperature (HPT) synthesis (Table 1), which raises the cost and difficulty of their preparation. It is thus essential to develop a relative "soft" method to reduce the synthesis pressure. An effective approach is to stabilize the high-pressure (HP) phase in an isostructural or structurally related matrix of an ambient-pressure (AP) prepared phase by chemical pressure, assisted with moderate physical pressure.[23,24] For instance, the multiferroic $CaMnTi_2O_6$ ($P4_2mc$) exhibits promising ferroelectric photovoltaic behavior but needs to be synthesized at 7 GPa.[25−27] However, Zhou et al. started from $Ca_{2-x}Mn_xTi_2O_6$ ($x \le 0.6$) and achieved the HP-$P4_2mc$ polymorph at a very modest pressure (0.1 GPa) with x = 0.6 ($Ca_{1.4}Mn_{0.6}Ti_2O_6$), which demonstrates similar multiferroic properties compared with $CaMnTi_2O_6$.[24] Chemically, the preparation of $Ca_{2-x}Mn_xTi_2O_6$ resembles intergrowth of $MnTiO_3$ in the $CaTiO_3$ host to form a solid solution of $(CaTiO_3)_{2-x}-(MnTiO_3)_x$, in which Ca^{2+} and Mn^{2+} have the same charge and similar ionic radii ($^{VIII}r(Ca^{2+})$ = 1.12 Å, $^{VIII}r(Mn^{2+})$ = 0.96 Å).[28] Accordingly, the chemical enhancement together with a moderate physical pressure (0.1 GPa) can underpin the polar HP-polymorph in $Ca_{2-x}Mn_xTi_2O_6$. Further SHG measurements confirmed that the polar phase can be stabilized with $0.4 \le x \le 0.6$, suggesting that Ca^{2+} and Mn^{2+} are disordered before the A-site columnar-ordering occurs at x above 0.4.[24] With increasing x, the ilmenite $MnTiO_3$ ($R\bar{3}$) phase would be expected, which can transfer into the polar LN-type structure ($R3c$) when reacted at 7 GPa. Accordingly, one may note $Pbnm$ ($CaTiO_3$, $x < 0.4$)−$P4_2mc$ ($CaMnTi_2O_6$)−$R3c$ ($MnTiO_3$, $1 < x < 2.0$) phase transitions in $Ca_{2-x}Mn_xTi_2O_6$ upon heating at 7 GPa. $MnTaO_2N$ is, to the best of our knowledge, the first and the only LN-type polar magnet in the oxynitride family,[15,29] which can be synthesized under 7.5 GPa with impurity phases even reacted at temperature as high as 1973 K. Recently, Inaguma et al. have intensively studied the $(MnTaO_2N)_{1-x}-(Mn_4Ta_2O_9)_x$ (x = 0.00−1.00) system, where the corundum-related $Mn_4Ta_2O_9$

Received: December 6, 2019
Revised: January 28, 2020
Published: January 29, 2020

https://dx.doi.org/10.1021/acs.chemmater.9b05051
Chem. Mater. 2020, 32, 1618−1626

Table 1. LN-Type Compounds Obtained by High-Pressure Synthesis

compound	synthetic condition	physical properties	refs.
$PbNiO_3$	3 GPa, 1073 K	AFM ($T_N \approx 205$ K)	12
$BiGa_{0.2}Fe_{0.8}O_3$	6 GPa, 1700 K	FM ($T_C \approx$ RT)	13
$BiGa_{0.4}Cr_{0.6}O_3$	6 GPa, 1700 K	AFM ($T_N \approx 56$ K)	13
$LiOsO_3$	6 GPa, 1473 K	ferroelectric metal	14
$MnTaO_2N$	6 GPa, 1673 K	nontrivial helical spin order ($T_N \approx 25$ K)	15
$ScFeO_3$	6 GPa, 1773 K	multiferroics ($T_N \approx 356$ K)	16
$GaFeO_3$	6 GPa, 1200 K	FM ($T_C \approx 408$ K)	17
$CuTaO_3$	6.5 GPa, 1273−1473 K	semiconductor	18
$MnTiO_3$	7 GPa, 973 K	AFM[d] ($T_N \approx 25$ K)[e]	4
$MnSnO_3$	7 GPa, 1073 K	AFM ($T_N \approx 53$ K)	4
$ZnSnO_3$	7 GPa, 1273 K	ferroelectric ($P_S \approx 47\ \mu$ C/cm^2)	19
Mn_2FeMO_6[a]	7 GPa, 1573 K	AFM ($T_N \approx 90$ K), pyroelectric	7
$PbZnO_3$	7.5 GPa, 1273−1473 K	diamagnetic metal	20
Zn_2FeTaO_6	9 GPa, 1623 K	AFM ($T_N \approx 22$ K)	21
$InFeO_3$	15 GPa, 1723 K	AFM ($T_N \approx 545$ K)	22
$ZnTiO_3$	16.5 GPa, 1423 K	large P_S[f] $\approx 75\ \mu$C/cm^2	5
$FeTiO_3$	18 GPa, 1473 K	FM[b] multiferroics ($T_C \approx 120$ K)[c]	1

[a]M = Nb, Ta. [b]Ferromagnetic. [c]Ferromagnetic Curie temperature T_C. [d]AFM. [e]AFM Néel temperature T_N. [f]Spontaneous polarization P_S.

($P\bar{3}c1$) can be prepared at AP and preserves the similar atomic arrangement as in $MnTaO_2N$.[30] It was found that the impurity phases can be largely suppressed at 7.5 GPa and 1573 K, and the LN-type pure phase was achieved for $x = 0.25$ ($Mn(Mn_{1/6}Ta_{5/6})O_{2.5}N_{0.5}$).[23] In this case, chemical pressure stabilizes the HP-polymorph at lower temperatures to obtain a pure phase. Chemical pressure can facilitate the formation of a HP-phase at lower pressure and/or temperature and provide a soft way to synthesize and scale up the HP phase.

The discovery of Mn_2FeMO_6 (M = Nb, Ta) for the first time extended the LN-type phase to double $A_2BB'O_6$ family with a second-order Jahn−Teller d^0-cation at the B′-site.[7,21] Mn_2FeMO_6 displays large spontaneous polarization (P_S) comparable to that of $BaTiO_3$ and an antiferromagnetic (AFM) transition around 90 K with short-range magnetic ordering up to ∼200 K. At lower temperatures, a pyroelectric response was also observed in Mn_2FeMO_6.[23] However, the stringent recipe conditions (7 GPa under 1573 K) radically limited potentially practical applications of Mn_2FeMO_6. In this work, we systematically investigate the $(Li_{1-x}Mn_x)$-$(Fe_{x/2}Nb_{1-x/2})O_3$ (x = 0.18, 0.33, 0.46, 0.57) system to stabilize the Mn_2FeNbO_6 phase in the isostructural $LiNbO_3$ matrix ($LiNbO_3$−Mn_2FeNbO_6) by chemical pressure or/and softer physical pressure at lower temperature and extensively characterize the evolution of crystal structure and magnetic properties. Possible approaches for future property optimization are also outlined.

2. EXPERIMENTAL DETAILS

2.1. Synthesis. $(Li_{1-x}Mn_x)(Fe_{x/2}Nb_{1-x/2})O_3$ (x = 0.18, 0.33, 0.46, 0.57) were prepared from stoichiometric mixtures of MnO (99.99%, Alfa Aesar), Fe_2O_3 (99.99%, Alfa Aesar), Nb_2O_5 (99.99%, Aladdin), and $LiNbO_3$. $LiNbO_3$ was first synthesized by heating a stoichiometric mixture of Li_2CO_3 (99.99%, Aladdin) and Nb_2O_5 (99.99%, Aladdin) at 1273 K for 12 h.[31] The x = 0.18 sample was synthesized under a 99.999%-Ar atmosphere at AP, while the $x \geq 0.2$ series was synthesized under HP. Stoichiometric mixtures of MnO, Fe_2O_3, Nb_2O_5, and $LiNbO_3$ were thoroughly mixed before being placed into a Pt capsule loaded into a Al_2O_3 crucible, pressurized typically over 2−5 h and reacted at 1373−1573 K under 1−5 GPa (1−2 GPa in piston cylinder press and 4−5 GPa in multi-anvil press) for 30 min before being quenched to room temperature (RT) by turning off the voltage supply to the resistance furnace.[32] The temperature was reduced to around RT in a few seconds. The pressure is maintained during the temperature quenching and then decompressed slowly.

2.2. Powder Crystal X-ray Diffraction and Chemical Analyses. All products were initially characterized by laboratory powder X-ray diffraction (PXD) in a RIGAKU D-MAX diffractometer (2200 VPC, Cu Kα, λ = 1.5418 Å) for phase identification and purity examination. In situ variable temperature PXD (VT-PXD) data were collected over a 2θ range of 20−60° from 300 to 800 K under a N_2 atmosphere (99.999%). RT synchrotron PXD (RT-SPXD) data were collected at AP on beamline BL14B at the Shanghai Synchrotron Radiation Facility (SSRF).[33,34] Rotating capillary modes were used to eliminate possible preferred orientation effects. A Mythen1K detector was used for high-quality data acquisition, and the wavelength (λ = 0.6900 Å) was obtained using Al_2O_3 standard. Rietveld analyses of SPXD data were performed using the software Topas-Academic V6.[35] Energy-dispersive spectroscopy (EDS) was measured on a JEOL JSM-7000F instrument with working parameters: 15 kV, 1 nA, detection range 0−20 keV, accumulation time 60 s.

2.3. Magnetic Properties Measurements. Magnetization response was measured on a Quantum Design PPMS instrument. The susceptibility was measured in zero-field cooled (ZFC) and FC conditions under an applied field of 0.05 T, in the temperatures range between 300 and 800 K. The isothermal magnetization curves were measured between −5 and 5 T at 300, 500, and 800 K, respectively.

2.4. In Situ Variable-Temperature SPXD Measurements. In situ variable temperature SPXD (VT-SPXD) data were collected at AP on the beamline BL14B at the SSRF (λ = 0.8857 Å). The polycrystalline powder was loaded into a vacuum sealed glass capillary (diameter ≈ 0.5 mm) and measured at 300, 408, 433, 453,473, 483; 503−603 K in steps of 20, and 800 K. Each scan was collected with 2θ between 1 and 53° and lasted approximately 45 min, following 5 min of thermal equilibration, to extract the lattice parameter evolution upon heating. The 300 K data were collected for comparison after cooling down from 800 K with a cooling rate of 20 K/min.

3. RESULTS AND DISCUSSION

3.1. Synthesis and Crystal Structure Evolution. The phase boundary of the synthesis of $(Li_{1-x}Mn_x)$ $(Fe_{x/2}Nb_{1-x/2})$-O_3 by chemical and physical pressure is illustrated in Figure S1. Chemical pressure is insufficient to stabilize the HP-phase for x above 0.33 unless intermediate physical pressure is set as 1, 2, and 5 GPa for x = 0.33, 0.46, 0.57, respectively. LN-type compounds were obtained for x = 0.18, 0.33, 0.46, 0.57, showing that HP-Mn_2FeNbO_6 contents have been successfully stabilized by chemical pressure at lower temperature and physical pressure than were needed to be applied in Mn_2FeNbO_6 (x = 1, 1573 K, 7 GPa).[7] Figure 1a presents the PXD patterns of $(Li_{1-x}Mn_x)$ $(Fe_{x/2}Nb_{1-x/2})O_3$ (x = 0.18, 0.33, 0.46, 0.57) synthesized at various temperatures and pressures. All PXD data can be well indexed with the $R3c$ space group. The peaks systematically shift (left) toward lower angles with increasing x as highlighted in Figure 1b, which suggests the growth of cell volume and successful formation of solid solution arising from the ionic radii difference between Mn^{2+} and Li^+ [in octahedral coordination, $^{VI}r(Mn^{2+}) = 0.83$ Å (high spin), $^{VI}r(Li^+) = 0.76$ Å)] and given the almost identical ionic radii of the B-site cations [$^{VI}r(Fe^{3+}) = 0.645$ Å (high spin) and $^{VI}r(Nb^{5+}) = 0.64$ Å].[28] The detailed chemical formulae are

https://dx.doi.org/10.1021/acs.chemmater.9b05051
Chem. Mater. 2020, 32, 1618−1626

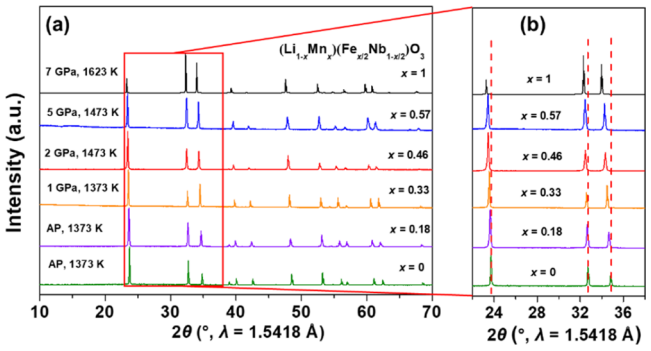

Figure 1. (a) PXD patterns for $(Li_{1-x}Mn_x)$ $(Fe_{x/2}Nb_{1-x/2})O_3$ (x = 0, 0.18, 0.33, 0.46, 0.57, 1), the pressure and temperature on the left represent the synthetic conditions. (b) Enlarged area illustrates the peak evolution with increasing Mn content. Dash lines are applied to highlight the peak position shift.

given in Table 2. The structural formula can be written as $(Li_{0.43}Mn_{0.57})$ $(Fe_{0.28}Nb_{0.72})O_3$ in the x = 0.57 case, in which the A-site is already dominated by Mn^{2+} (57%). Gram-level specimens of $(Li_{0.43}Mn_{0.57})$ $(Fe_{0.28}Nb_{0.72})O_3$ can be synthesized at 5 GPa, instead of milligram-scale yields of Mn_2FeNbO_6 driven at 7 GPa in our high-pressure apparatus. SEM and EDS measurements (Figure S2) confirmed the homogeneity and composition of the as-made samples (x = 0.18, 0.33, 0.46, 0.57) at micrometer scale. The composition measured by EDS corresponds well with the feed ratio except for x = 0.18, which have too low a content of Fe and Mn compared to Nb. Figure 2 depicts the Rietveld refinement results of $(Li_{1-x}Mn_x)$ $(Fe_{x/2}Nb_{1-x/2})O_3$ (x = 0.18, 0.33, 0.46, 0.57) with the inset showing the crystal structure for x = 0.18 in Figure 2a. All phases can be well fitted in a LN-based structural model as listed in Table 2, and the cationic occupation rates were fixed according to the nominal composition during the refinements. Figure 3a,b shows the evolution of refined unit-cell parameters of as-made $(Li_{1-x}Mn_x)$ $(Fe_{x/2}Nb_{1-x/2})O_3$ (x = 0, 0.18, 0.33, 0.46, 0.57, 1). The unit-cell-parameter evolution loosely follows Vegard's law and increases roughly linearly with the compositional content of the Mn-bearing HP-phase Mn_2FeNbO_6.[36] The crystal structure of $(Li_{1-x}Mn_x)$ $(Fe_{x/2}Nb_{1-x/2})O_3$ exemplified by x = 0.18 (inset of Figure 2a) contains face- and edge-sharing $(Li_{0.82}/Mn_{0.18})O_6$–$(Fe_{0.09}/Nb_{0.91})O_6$ octahedra along the c-axis and in the ab-plane, respectively. The calculated bond valence sums, octahedral distortion parameter (Δ),[37] and P_S[38] are summarized in Tables S1–S4.

The unit cell evolution in Figure 3a,b is accompanied by local structure relaxation within face-sharing octahedral pairs. The two kinds (three short and three long) of A-O distances are very anisotropic for x = 0.18, reading 2.680(4) and 1.959(1) Å (Table S1), respectively. The low Mn content (18%) at the A-site is insufficient to affect the distortion, and Li/Mn atoms are almost seated in the plane of the three short-bonded O atoms (Figure 4a) as observed for Li atoms in LN, giving large $\Delta_{Li/Mn}$ of 242.3 × 10^{-4} and $d_{Li/Mn}$ of 0.93(1) Å. For x = 0.33, 0.46, and 0.57, the <Li/Mn–O> bond length [2.175(5)–2.182(4) Å] elongates with the increasing Mn content at the A site and approaches that in Mn_2FeNbO_6 (2.19(1) Å). The $(Li/Mn)O_6$ octahedra are less distorted with $d_{Li/Mn}$ averaged to around 0.5 Å (Figure 4b–d). The $(Fe/Nb)O_6$ octahedral distortion degree is more regular for all x values with (Fe/Nb)–O distance between 1.897(1)–1.987(4) Å and 2.067(4)–2.117(3) Å for shorter and longer (Fe/Nb)–O bonds, respectively. The P_S along the c-axis was calculated to be 18.2, 63.3, 53.1, and 54.1 $\mu C/cm^2$ for x = 0.18, 0.33, 0.46, 0.57, respectively. Apparently, the incorporation of Mn^{2+}–Fe^{3+} into the Li^+–Nb^{5+} sites in LN lowers the charge difference and weakens the static electron repulsion between the face-sharing A- and B-sites, thus allowing closer approach of the A-site cation toward the octahedral centroid and enhancing magnetic interactions.

3.2. Magnetic Properties of As-Made Samples. Figure 5 shows the temperature dependence of magnetization, magnetic susceptibility (χ^{-1}) curves of the as-made $(Li_{1-x}Mn_x)$ $(Fe_{x/2}Nb_{1-x/2})O_3$. All samples show RT ferromagnetism rather than the AFM ordering in Mn_2FeNbO_6 ($T_N \approx$ 90 K), which can be attributed to short-ranged exchange interactions by inducting nanoscale clusters of magnetic impurities in diluted magnetic systems ($LiNbO_3$–Mn_2FeNbO_6).[39] The ZFC and FC curves split around 600, 670, 650, and 550 K for x = 0.18, 0.33, 0.46, 0.57, respectively. ZFC and FC show "loop"-like curves for x = 0.33 and 0.46, which aroused our great interest. The high-temperature curves were fitted with a simple Curie

Table 2. Comparison of Refined Structural Parameters of $(Li_{1-x}Mn_x)$ $(Fe_{x/2}Nb_{1-x/2})O_3$ (x = 0, 0.18, 0.33, 0.46, 0.57, 1.00) collected at RT in ABO_3 form

x	0	0.18	0.33	0.46	0.57	1
formula	$LiNbO_3$	$(Li_{0.82}Mn_{0.18})$ $(Fe_{0.09}Nb_{0.91})O_3$	$(Li_{0.67}Mn_{0.33})$ $(Fe_{0.17}Nb_{0.83})O_3$	$(Li_{0.54}Mn_{0.46})$ $(Fe_{0.23}Nb_{0.77})O_3$	$(Li_{0.43}Mn_{0.57})$ $(Fe_{0.28}Nb_{0.72})O_3$	$MnFe_{0.5}Nb_{0.5}O_3$
a (Å)	5.14929(4)	5.17589(4)	5.19699(1)	5.22485(3)	5.23421(3)	5.2740(1)
c (Å)	13.8606(1)	13.8666(1)	13.87683(4)	13.9028(1)	13.9150(1)	13.9338(2)
v (Å^3)	318.281(7)	321.717(7)	324.583(2)	328.687(6)	330.156(5)	335.65(1)
A_z	0.216(1)	0.2203(2)	0.2200(1)	0.21762(9)	0.21703(7)	0.219(1)
A_{occ}	1	0.82/0.18	0.67/0.33	0.54/0.46	0.43/0.57	0/1
A_{Biso} (Å^2)	2.41(4)	1.85(6)	1.51(4)	1.06(4)	0.87(7)	0.42(2)
B_{occ}	1	0.91/0.09	0.833/0.167	0.77/0.23	0.71/0.29	0.5/0.5
B_{Biso} (Å^2)	1.81(3)	0.62(1)	0.88(1)	0.99 (2)	0.95 (2)	0.42(2)
O_x	0.017(1)	0.0498(5)	0.0323(5)	0.0339(6)	0.0301(7)	0.034(2)
O_y	0.372(1)	0.3483(9)	0.3200(6)	0.3117(6)	0.3131(6)	0.315(3)
O_z	0.0542(5)	0.0701(1)	0.1024(2)	0.0972(4)	0.0970(5)	0.120(1)
O_{Biso} (Å^2)	2.4(1)	0.94(4)	0.20(3)	0.12(4)	0.85(3)	0.42(2)
R_{wp}	10.4%	9.71%	5.91%	6.86%	6.43%	10.4%
R_p	7.8%	7.10%	7.29%	9.36%	7.87%	7.8%

https://dx.doi.org/10.1021/acs.chemmater.9b05051
Chem. Mater. 2020, 32, 1618–1626

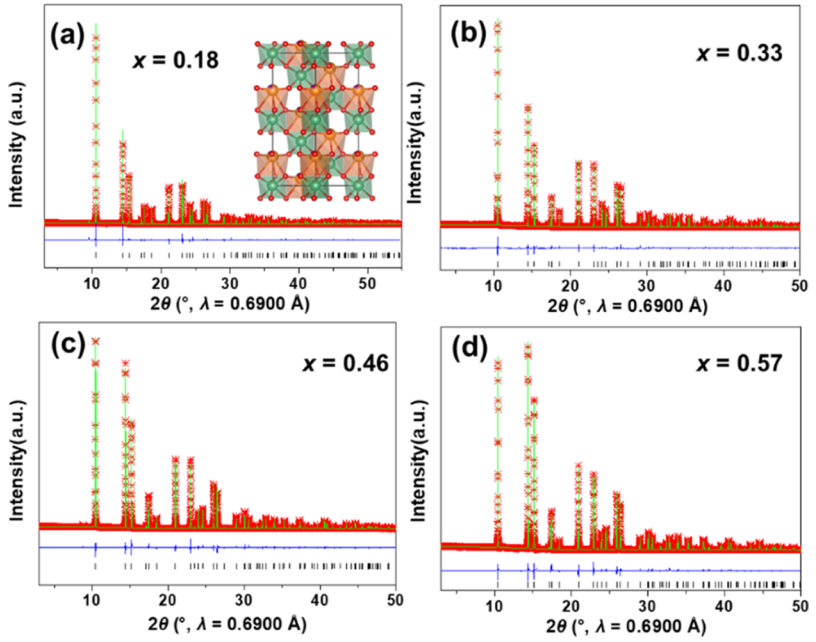

Figure 2. Rietveld refinement of the SPXD data for $(Li_{1-x}Mn_x)$ $(Fe_{x/2}Nb_{1-x/2})O_3$. (a) x = 0.18; (b) x = 0.33; (c) x = 0.46; (d) x = 0.57; the red cross represents the calculated fit, the green line the observed data, the deep blue line the difference, black tick marks the peak positions. Inset of Figure 2a shows the crystal structure viewed along [110] direction in the x = 0.18 case. Mn/Li, purple/orange spheres; $(Fe/Nb)O_6$ octahedra, green; O, red spheres.

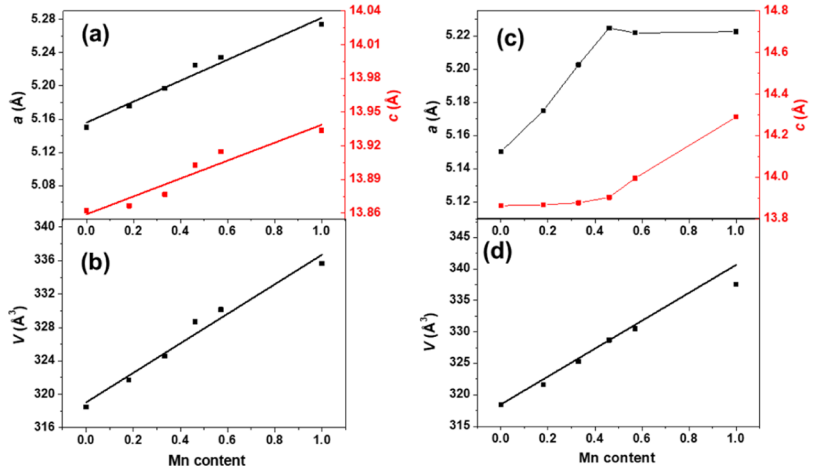

Figure 3. Evolution of the lattice parameters extracted from $(Li_{1-x}Mn_x)$ $(Fe_{x/2}Nb_{1-x/2})O_3$ (x = 0, 0.18, 0.33, 0.46, 0.57, 1). (a,b) as made; (c,d) annealed at 800 K.

formula: $\chi = \chi_0 + C/(T - \theta)$. The Curie–Weiss (CW) temperatures (θ) and Curie constants (C) were θ_{ZFC} = 284.5 K, θ_{FC} = 257.3 K; θ_{ZFC} = 77.1 K, θ_{FC} = 66.9 K and C_{ZFC} = 1.54, C_{FC} = 1.59, and C_{ZFC} = C_{FC} = 2.43 for x = 0.33 and 0.46, respectively. The fitting allowed us to extract the value of the effective magnetic moment $\mu_{eff\text{-}ZFC}$ = 3.51 μ_B, $\mu_{eff\text{-}FC}$ = 3.56 μ_B, and $\mu_{eff\text{-}ZFC}$ = $\mu_{eff\text{-}FC}$ = 4.41 μ_B for x = 0.33 and 0.46, respectively, which are more than the calculated magnetic moment, μ_{eff} = 2.78 μ_B (x = 0.33) and μ_{eff} = 3.84 μ_B (x = 0.46), suggesting enhanced magnetic interplays from possibly local atomic aggregation of magnetically active transition-metal ions. The magnetic transition temperatures in FC measurements are systematically around 30 K lower than those from ZFC plots in Figure 5. The "loop"-like curves for x = 0.33 and 0.46 overlap-cross the ZFC and FC plots for x = 0.18 and 0.57, indicating possible phase transition of the as-made specimen when heated up to 800 K in the ZFC measurements. To get clearer insights, in situ VT-SPXD measurements were thus conducted on selected samples.

3.3. In Situ VT-SPXD. In order to reveal the internal changes of the sample in the heating process up to 800 K during the magnetic measurements, we selected the x = 0.46 sample $(Li_{0.54}Mn_{0.46})$ $(Fe_{0.23}Nb_{0.77})O_3$ for in situ VT-SPXD and PXD measurements (Figures S3–S5). The T_{ZFC} and T_{FC} of x = 0.46 show the most significant difference (41 K) among the four compounds. The refined crystal structure details are given in Tables S5 and S6. As can be seen in Figure 6, the cell parameters extracted from VT-SPXD data increase linearly with the increase of temperature between 300 and 550 and 600–800 K; however, a near-zero thermal expansion plateau (ZTE) of the c-axis appears around the magnetic transition temperature between 550 and 600 K, which can be attributed

https://dx.doi.org/10.1021/acs.chemmater.9b05051
Chem. Mater. 2020, 32, 1618–1626

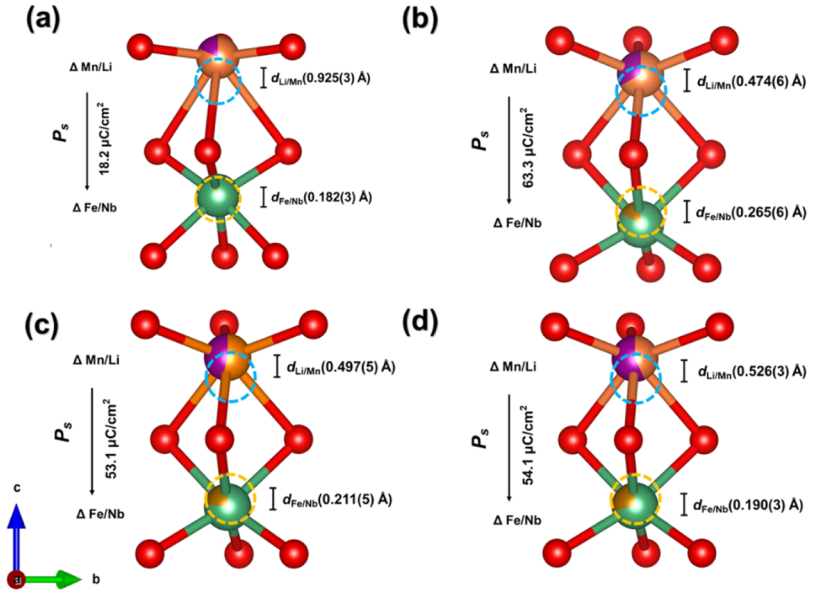

Figure 4. Local structure of the face-sharing $(Li/Mn)O_6/(Fe/Nb)O_6$ octahedral pairs of (a) $x = 0.18$, (b) $x = 0.33$, (c) $x = 0.46$, and (d) $x = 0.57$. The atomic displacements (d_s) away from the $(Li/Mn)O_6$ and $(Fe/Nb)O_6$ octahedral centroids (highlighted by dashed circles) are indicated as $d_{Li/Mn}$ and $d_{Fe/Nb}$, respectively. P_S is for the spontaneous polarization.

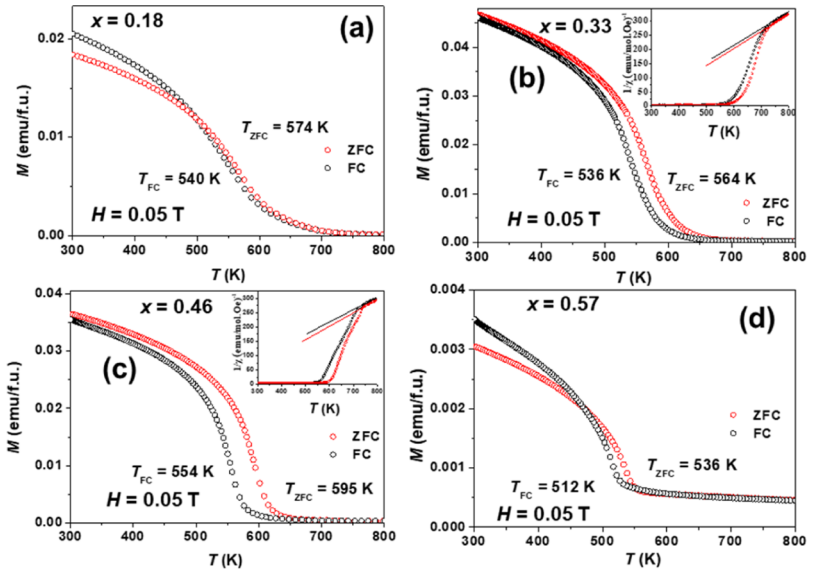

Figure 5. (a–d) Magnetic behavior of $(Li_{1-x}Mn_x)(Fe_{x/2}Nb_{1-x/2})O_3$ ($x = 0.18, 0.33, 0.46, 0.57$) at 0.05 T, inset shows the susceptibility inverse ($1/\chi$) versus temperature plots, the black and red line displays the CW fitting.

to magnetostriction as shown in Figure S6. Analysis of the 300 K measurements after cooling down from the in situ VT-SPXD (Figure 6a,b) indicates that c becomes 0.0049 Å longer than that of the as-made sample, while the cell dimension (0.04 Å larger) and ab-plane remains similar (0.0006 Å smaller). Similar phenomena have been reported in double-corundum multiferroic Mn_2FeMoO_6 and Mn_2MnWO_6 attributed to cationic rearrangement and magnetostriction.[6,9] To further explore the unusual dimensional expansion along the c-axis and slight shrinking in the ab-plane, we compared the temperature-dependent (Li/Mn)−O (Figure 6c) and (Fe/Nb)−O (Figure 6d) bond length evolution. In $(Li_{0.54}Mn_{0.46})(Fe_{0.23}Nb_{0.77})O_3$, below 453 K, the long bond in (Li/Mn)−O becomes longer and short bond becomes shorter with temperature increasing. Above 453 K, the fluctuation of the (Li/Mn)−O bond distance decreases and transits into a plateau stage. For the annealed sample, the (Li/Mn)−O bond lengths do not recover the as-made state. The long bond becomes longer and shorter bond becomes shorter than the as-made at 300 K. In contrast, the (Fe/Nb)−O bond lengths approximately returned to the initial state after cooling to 300 K. Figure 7 shows that Li atoms nearly locate on the triangle oxygen plane of pure LiO_6 octahedral in LN, while Mn atoms are closer to the MnO_6 octahedron center in Mn_2FeNbO_6.[7] Accordingly, the increment of the Mn content in the $(Li/Mn)O_6$ octahedra gradually restrains small $d_{Li/Mn}$ values from the octahedral centroids (highlighted by dashed circles). In $x = 0.46$ case, $d_{Li/Mn}$ in the as-made sample [0.45 (1) Å] was elongated to 0.55(1) Å at 800 K by overcoming the magnetostriction effect. Upon cooling, the magnetoelastic (if any) and thermal effects were

https://dx.doi.org/10.1021/acs.chemmater.9b05051
Chem. Mater. 2020, 32, 1618−1626

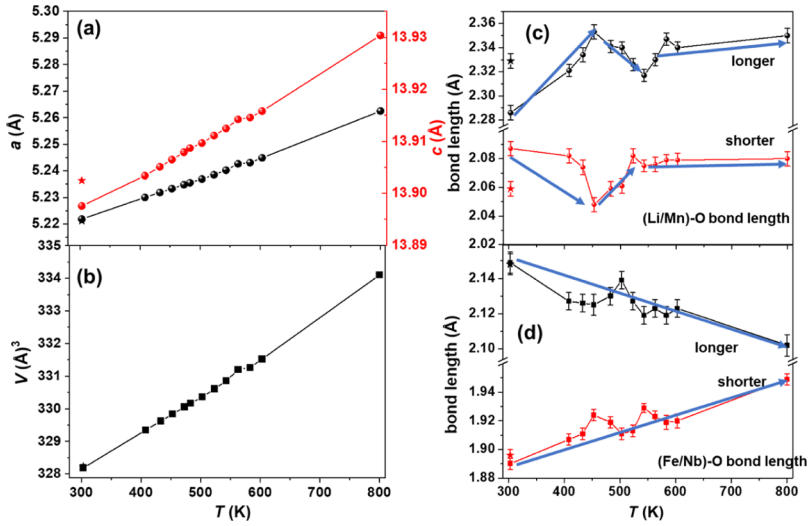

Figure 6. Lattice parameter (a,b) and bond lengths (c,d) evolution from 300 to 800 K in vacuum for $(Li_{0.54}Mn_{0.46})$ $(Fe_{0.23}Nb_{0.77})O_3$. The Asterisks (*) in (a,b) represent the data extracted from 300 K measurements after cooling down from 800 K. Unlike (Fe/Nb)−O bond lengths in (d), the longer and shorter (Li/Mn)−O bond lengths (c) did not recover the original state at 300 K after cooling from 800 K compared with that in the as-made sample at 300 K. The blue arrow is the trend line in (c,d).

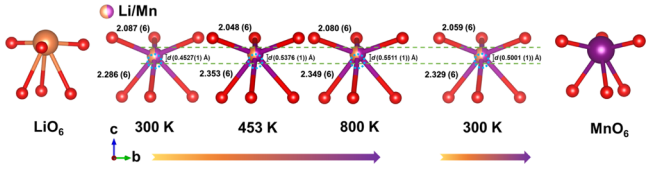

Figure 7. Schematic illustrations with respect to $(Li/Mn)O_6$ octahedra of $(Li_{0.54}Mn_{0.46})$ $(Fe_{0.23}Nb_{0.77})O_3$ refined from in situ VT-SPXD. The structural information of LiO_6 and MnO_6 octahedra are from LN and Mn_2FeNbO_6, respectively.

not strong enough to squeeze the Li/Mn back to the original state with the absence of physical pressure and thus rendered ~0.05(1) Å larger $d_{Li/Mn}$ [0.50(1) Å] (Figure 7) compared to that of the as-made sample. The structural relaxation along *c*-axis increased the distance between (Li/Mn) and (Fe/Nb) within the face-sharing octahedral pairs after annealing, which weakens the magnetic interactions and is responsible for the magnetic transition temperature drop in the FC curves in Figure 5.

In situ VT-SPXD studies on $x = 0.46$ sample indicate that a near ZTE plateau around the magnetic transition temperatures is present in $(Li_{1-x}Mn_x)$ $(Fe_{x/2}Nb_{1-x/2})O_3$ owing to the competition between the thermal effect and magnetostriction. Accordingly, significant *x*-dependent evolution of structural relaxation is expected in the whole $(Li_{1-x}Mn_x)$ $(Fe_{x/2}Nb_{1-x/2})$-O_3 series, especially for the higher *x* value cases. Figure 3c,d presents the diagram of unit cell evolution to the Mn content at A-sites at RT after annealing the samples at 800 K. The unit-cell volume increases linearly accompanied by a linear increase of *a* and *c* when the Mn content is below 60% but deviates below the fitting line at higher Mn content. The cell dimension

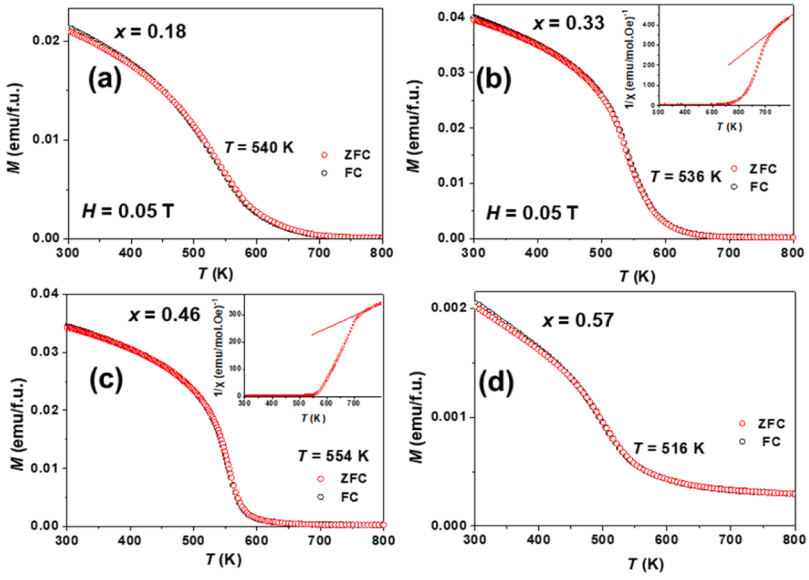

Figure 8. Temperature-dependent magnetization ZFC and FC curves of annealed $(Li_{1-x}Mn_x)$ $(Fe_{x/2}Nb_{1-x/2})O_3$ ($x = 0.18, 0.33, 0.46, 0.57$) at 0.05 T. Inset shows the susceptibility inverse ($1/\chi$) versus temperature plots, the red line display the CW fitting.

https://dx.doi.org/10.1021/acs.chemmater.9b05051
Chem. Mater. 2020, 32, 1618−1626

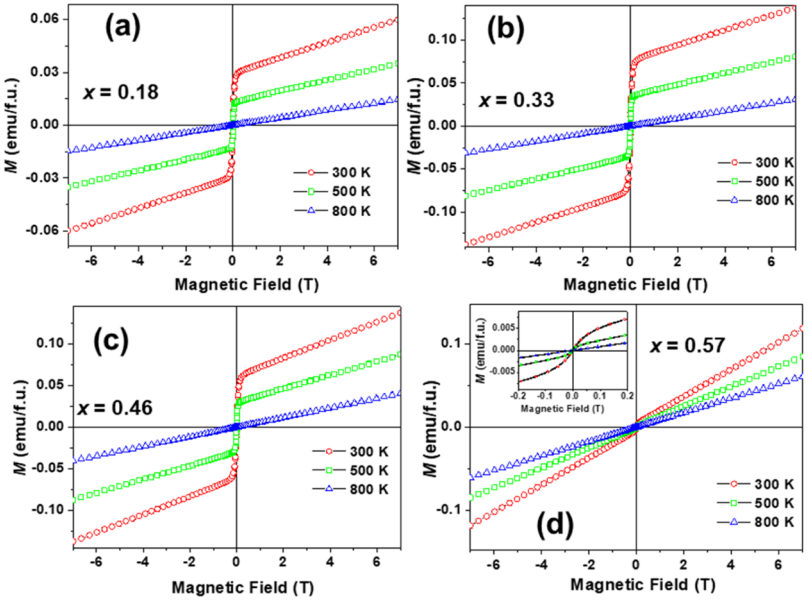

Figure 9. Isothermal magnetization plots of annealed $(Li_{1-x}Mn_x)$ $(Fe_{x/2}Nb_{1-x/2})O_3$ (x = (a) 0.18, (b) 0.33, (c) 0.46, (d) 0.57). Inset of (d) shows the enlarged area between −0.2 and 0.2 T.

in the *ab*-plane reaches a maximum at 50%-Mn and then drops a little bit and almost remains constant with Mn-content above 50%, whereas *c* shows increasing growth with increasing Mn content. Compared to the as-made Mn_2FeNbO_6, the *c*-axis expanded ∼0.355 (1) Å after annealing. These findings suggest that the magnetostriction effect plays a more critical rule in the Mn-rich cases to maintain a compacted cell and strong magnetic interactions. Once the magnetostriction was weakened, the more the Mn-content, the larger the structural relaxation along the *c*-axis, and this relaxation is irreversible with the absence of physical pressure. Therefore, magnetic measurements on the annealed (relaxed) samples were conducted to eliminate the "loops", magnetic transition discrepancy, and overlap-cross in Figure 5.

3.4. Magnetic Properties of Annealed Samples. After the first round of magnetic measurements, we subsequently conducted another cycle as shown in Figure 8a−d. The ZFC and FC are coincident for x = 0.18, 0.33, 0.46, 0.57 as expected, in good agreement with the in situ VT-SPXD results. Therefore, in Figure 5, the ZFC and FC curves correspond to the as-made and annealed (relaxed) samples, respectively. The CW fitting result: θ = 354.7 K; θ = 142.1 K and C_{ZFC} = 0.99, C_{FC} = 1.89 for x = 0.33 and 0.46, respectively. The effective magnetic moments were μ_{eff} = 2.81 μ_B and μ_{eff} = 3.88 μ_B for x = 0.33 and 0.46, respectively, which correspond well with the calculated magnetic moment, μ_{eff} = 2.78 μ_B (x = 0.33) and, μ_{eff} = 3.84 μ_B (x = 0.46). Figure 9a−d presents the isothermal magnetization (M) versus H curves of $(Li_{1-x}Mn_x)$ $(Fe_{x/2}Nb_{1-x/2})O_3$ (x = 0.18, 0.33, 0.46, 0.57) recorded at 300, 500, and 800 K after measuring the temperature dependence of magnetization. At 800 K, samples were in the paramagnetic state, whereas at 300 and 500 K, specimens show typically ferromagnetic behavior for x = 0.18, 0.33, 0.46 and ferrimagnetic behavior for x = 0.57.

4. CONCLUSIONS

In summary, the higher-pressure made (7 GPa and 1573 K) Mn_2FeNbO_6 phase can be stabilized in the $LiNbO_3$ matrix (Mn_2FeNbO_6−$LiNbO_3$) at 1373−1493 K between 0 and 5 GPa in large scale (gram level) for each batch, resulting in above-room-temperature $LiNbO_3$-type polar magnets $(Li_{1-x}Mn_x)$ $(Fe_{x/2}Nb_{1-x/2})O_3$ (x = 0.18, 0.33, 0.46, and 0.57 at 0, 1, 2, and 5 GPa, respectively). The $(Li_{1-x}Mn_x)$ $(Fe_{x/2}Nb_{1-x/2})O_3$ series exhibit ferromagnetic ordering temperature between 510 and 550 K and spontaneous polarization around 18−63 $\mu C/cm^2$. The competition between the thermal effect and magnetostriction resulted in *c*-axis near-zero thermal expansion around the magnetic ordering temperature region upon heating at ambient pressure. The irreversible structural relaxation along the *c*-axis after annealing led to around 30 K lowering of magnetic transition temperatures but still well above RT. Further work is expected to grow large single crystals for multiferroic characterization. The significantly lowering of synthesis temperature and pressure for $(Li_{1-x}Mn_x)$ $(Fe_{x/2}Nb_{1-x/2})O_3$ compared with those for Mn_2FeNbO_6 is attributed to chemical pressure effect. The design and preparation of $(Li_{1-x}Mn_x)$ $(Fe_{x/2}Nb_{1-x/2})O_3$ suggests an effective strategy to drive the HP phase by the combination of chemical pressure and intermediate physical pressure and paves the way for large-scale and low-cost stabilization of HP phases.

■ ASSOCIATED CONTENT

Supporting Information

The Supporting Information is available free of charge at https://pubs.acs.org/doi/10.1021/acs.chemmater.9b05051.

PXD patterns showing the phase boundary of chemical and physical pressure driving synthesis; SEM and EDS results; refinements and analyses of the in situ VT-SPXD data; crystallographic tables; and crystallographic information file for $(Li_{1-x}Mn_x)$ $(Fe_{x/2}Nb_{1-x/2})O_3$ (x = 0.18, 0.33, 0.46, 0.57) (PDF)

Crystallographic information for $(Li_{1-x}Mn_x)$ $(Fe_{x/2}Nb_{1-x/2})O_3$ (x = 0.18) and supporting crystallographic information file may also be obtained from FIZ Karlsruhe, 76344 Eggenstein-Leopoldshafen, Germany (e-mail: crysdata@fiz-karlsruhe.de), on quoting the deposition number: x = 0.18 (1969007), x = 0.33

https://dx.doi.org/10.1021/acs.chemmater.9b05051
Chem. Mater. 2020, 32, 1618−1626

(1969017), x = 0.46 (1969018), x = 0.57 (1969019) (CIF)

Crystallographic data for $(Li_{1-x}Mn_x)$ $(Fe_{x/2}Nb_{1-x/2})O_3$ (x = 0.33) (CIF)

Crystallographic data for $(Li_{1-x}Mn_x)$ $(Fe_{x/2}Nb_{1-x/2})O_3$ (x = 0.46) (CIF)

Crystallographic data for $(Li_{1-x}Mn_x)$ $(Fe_{x/2}Nb_{1-x/2})O_3$ (x =0.57) (CIF)

AUTHOR INFORMATION

Corresponding Author

Man-Rong Li − *Key Laboratory of Bioinorganic and Synthetic Chemistry of Ministry of Education, School of Chemistry, Sun Yat-Sen University, Guangzhou 510275, P. R. China;* orcid.org/0000-0001-8424-9134; Email: limanrong@mail.sysu.edu.cn

Authors

Yifeng Han − *Key Laboratory of Bioinorganic and Synthetic Chemistry of Ministry of Education, School of Chemistry, Sun Yat-Sen University, Guangzhou 510275, P. R. China*

Chuanhui Zhu − *Key Laboratory of Bioinorganic and Synthetic Chemistry of Ministry of Education, School of Chemistry, Sun Yat-Sen University, Guangzhou 510275, P. R. China*

Yi Peng − *Institute of Physics, Chinese Academy of Sciences, Beijing 100190, P. R. China*

Shufang Li − *Key Laboratory of Bioinorganic and Synthetic Chemistry of Ministry of Education, School of Chemistry, Sun Yat-Sen University, Guangzhou 510275, P. R. China*

MeiXia Wu − *Key Laboratory of Bioinorganic and Synthetic Chemistry of Ministry of Education, School of Chemistry, Sun Yat-Sen University, Guangzhou 510275, P. R. China*

Shuang Zhao − *Key Laboratory of Bioinorganic and Synthetic Chemistry of Ministry of Education, School of Chemistry, Sun Yat-Sen University, Guangzhou 510275, P. R. China*

Zheng Deng − *Institute of Physics, Chinese Academy of Sciences, Beijing 100190, P. R. China*

Changqing Jin − *Institute of Physics, Chinese Academy of Sciences, Beijing 100190, P. R. China*

Wei Du − *State Key Laboratory of Ore Deposit Geochemistry, Institute of Geochemistry, Chinese Academy of Sciences, Guiyang 550081, China*

David Walker − *Lamont Doherty Earth Observatory, Columbia University, Palisades, New York 10964, United States*

Complete contact information is available at: https://pubs.acs.org/10.1021/acs.chemmater.9b05051

Notes

The authors declare no competing financial interest.

ACKNOWLEDGMENTS

This work was financially supported by the National Science Foundation of China (NSFC-21875287, 21801253, 11804404, and 11874400), National Key R&D Program of China (2018YFA0305700), the Program for Guangdong Introducing Innovative and Entrepreneurial Teams (2017ZT07C069), the Key Research Program of Frontier Sciences of the Chinese Academy of Sciences (QYZDB-0S0S0W0-SLH013), and the CAS Interdisciplinary Innovation Team. The authors thank beamline BL14B1 (SSRF) for providing the beam time and helps during experiments.

REFERENCES

(1) Varga, T.; Kumar, A.; Vlahos, E.; Denev, S.; Park, M.; Hong, S.; Sanehira, T.; Wang, Y.; Fennie, C. J.; Streiffer, S. K.; Ke, X.; Schiffer, P.; Gopalan, V.; Mitchell, J. F. Coexistence of weak ferromagnetism and ferroelectricity in the high pressure $LiNbO_3$-type phase of $FeTiO_3$. *Phys. Rev. Lett.* **2009**, *103*, 047601.

(2) Arévalo-López, A. M.; Attfield, J. P. Weak ferromagnetism and domain effects in multiferroic $LiNbO_3$-type $MnTiO_3$-II. *Phys. Rev. B: Condens. Matter Mater. Phys.* **2013**, *88*, 104416.

(3) Son, J. Y.; Lee, G.; Jo, M.-H.; Kim, H.; Jang, H. M.; Shin, Y.-H. Heteroepitaxial Ferroelectric $ZnSnO_3$ Thin Film. *J. Am. Chem. Soc.* **2009**, *131*, 8386−8387.

(4) Aimi, A.; Katsumata, T.; Mori, D.; Fu, D.; Itoh, M.; Kyômen, T.; Hiraki, K.-i.; Takahashi, T.; Inaguma, Y. High-pressure synthesis and correlation between structure, magnetic, and dielectric properties in $LiNbO_3$-type $MnMO_3$ (M = Ti, Sn). *Inorg. Chem.* **2011**, *50*, 6392−6398.

(5) Ruiz-Fuertes, J.; Winkler, B.; Bernert, T.; Bayarjargal, L.; Morgenroth, W.; Koch-Muller, M.; Refson, K.; Milman, V.; Tamura, N. Ferroelectric soft mode of polar $ZnTiO_3$ investigated by Raman spectroscopy at high pressure. *Phys. Rev. B* **2015**, *91*, 214110.

(6) Li, M. R.; McCabe, E. E.; Stephens, P. W.; Croft, M.; Collins, L.; Kalinin, S. V.; Deng, Z.; Retuerto, M.; Sen Gupta, A.; Padmanabhan, H.; Gopalan, V.; Grams, C. P.; Hemberger, J.; Orlandi, F.; Manuel, P.; Li, W. M.; Jin, C. Q.; Walker, D.; Greenblatt, M. Magnetostriction-polarization coupling in multiferroic Mn_2MnWO_6. *Nat. Commun.* **2017**, *8*, 2037.

(7) Li, M.-R.; Walker, D.; Retuerto, M.; Sarkar, T.; Hadermann, J.; Stephens, P. W.; Croft, M.; Ignatov, A.; Grams, C. P.; Hemberger, J.; Nowik, I.; Halasyamani, P. S.; Tran, T. T.; Mukherjee, S.; Dasgupta, T. S.; Greenblatt, M. Polar and magnetic Mn_2FeMO_6 (M = Nb, Ta) with $LiNbO_3$-type structure: high-pressure synthesis. *Angew. Chem., Int. Ed. Engl.* **2013**, *52*, 8406−8410.

(8) Cai, G.-H.; Greenblatt, M.; Li, M.-R. Polar Magnets in Double Corundum Oxides. *Chem. Mater.* **2017**, *29*, 5447−5457.

(9) Li, M.-R.; Retuerto, M.; Stephens, P. W.; Croft, M.; Sheptyakov, D.; Pomjakushin, V.; Deng, Z.; Akamatsu, H.; Gopalan, V.; Sánchez-Benítez, J.; Saouma, F. O.; Jang, J. I.; Walker, D.; Greenblatt, M. Low-Temperature Cationic Rearrangement in a Bulk Metal Oxide. *Angew. Chem., Int. Ed.* **2016**, *55*, 9862−9867.

(10) Li, M.-R.; Croft, M.; Stephens, P. W.; Ye, M.; Vanderbilt, D.; Retuerto, M.; Deng, Z.; Grams, C. P.; Hemberger, J.; Hadermann, J.; Li, W.-M.; Jin, C.-Q.; Saouma, F. O.; Jang, J. I.; Akamatsu, H.; Gopalan, V.; Walker, D.; Greenblatt, M. Mn_2FeWO_6: A New Ni_3TeO_6-Type Polar and Magnetic Oxide. *Adv. Mater.* **2015**, *27*, 2177−2181.

(11) Li, M.-R.; Retuerto, M.; Walker, D.; Sarkar, T.; Stephens, P. W.; Mukherjee, S.; Dasgupta, T. S.; Hodges, J. P.; Croft, M.; Grams, C. P.; Hemberger, J.; Sánchez-Benítez, J.; Huq, A.; Saouma, F. O.; Jang, J. I.; Greenblatt, M. Magnetic-structure-stabilized polarization in an above-room-temperature ferrimagnet. *Angew. Chem., Int. Ed. Engl.* **2014**, *53*, 10774−10778.

(12) Inaguma, Y.; Tanaka, K.; Tsuchiya, T.; Mori, D.; Katsumata, T.; Ohba, T.; Hiraki, K.-i.; Takahashi, T.; Saitoh, H. Synthesis, Structural Transformation, Thermal Stability, Valence State, and Magnetic and Electronic Properties of $PbNiO_3$ with Perovskite- and $LiNbO_3$-Type Structures. *J. Am. Chem. Soc.* **2011**, *133*, 16920−16929.

(13) Belik, A. A.; Rusakov, D. A.; Furubayashi, T.; Takayama-Muromachi, E. $BiGaO_3$-Based Perovskites: A Large Family of Polar Materials. *Chem. Mater.* **2012**, *24*, 3056−3064.

(14) Shi, Y.; Guo, Y.; Wang, X.; Princep, A. J.; Khalyavin, D.; Manuel, P.; Michiue, Y.; Sato, A.; Tsuda, K.; Yu, S.; Arai, M.; Shirako, Y.; Akaogi, M.; Wang, N.; Yamaura, K.; Boothroyd, A. T. A ferroelectric-like structural transition in a metal. *Nat. Mater.* **2013**, *12*, 1024−1027.

(15) Tassel, C.; Kuno, Y.; Goto, Y.; Yamamoto, T.; Brown, C. M.; Hester, J.; Fujita, K.; Higashi, M.; Abe, R.; Tanaka, K.; Kobayashi, Y.; Kageyama, H. $MnTaO_2N$: Polar $LiNbO_3$-type Oxynitride with a Helical Spin Order. *Angew. Chem., Int. Ed.* **2015**, *54*, 516−521.

(16) Kawamoto, T.; Fujita, K.; Yamada, I.; Matoba, T.; Kim, S. J.; Gao, P.; Pan, X.; Findlay, S. D.; Tassel, C.; Kageyama, H.; Studer, A. J.; Hester, J.; Irifune, T.; Akamatsu, H.; Tanaka, K. Room-temperature polar ferromagnet $ScFeO_3$ transformed from a high-pressure orthorhombic perovskite phase. *J. Am. Chem. Soc.* **2014**, *136*, 15291−15299.
(17) Niu, H.; Pitcher, M. J.; Corkett, A. J.; Ling, S.; Mandal, P.; Zanella, M.; Dawson, K.; Stamenov, P.; Batuk, D.; Abakumov, A. M.; Bull, C. L.; Smith, R. I.; Murray, C. A.; Day, S. J.; Slater, B.; Cora, F.; Claridge, J. B.; Rosseinsky, M. J. Room Temperature Magnetically Ordered Polar Corundum $GaFeO_3$ Displaying Magnetoelectric Coupling. *J. Am. Chem. Soc.* **2017**, *139*, 1520−1531.
(18) Sleight, A. W.; Prewitt, C. T. Preparation of $CuNbO_3$ and $CuTaO_3$ at high pressure. *Mater. Res. Bull.* **1970**, *5*, 207−211.
(19) Inaguma, Y.; Sakurai, D.; Aimi, A.; Yoshida, M.; Katsumata, T.; Mori, D.; Yeon, J.; Halasyamani, P. S. Dielectric properties of a polar $ZnSnO_3$ with $LiNbO_3$-type structure. *J. Solid State Chem.* **2012**, *195*, 115−119.
(20) Mori, D.; Tanaka, K.; Saitoh, H.; Kikegawa, T.; Inaguma, Y. Synthesis, Direct Formation under High Pressure, Structure, and Electronic Properties of $LiNbO_3$-type Oxide $PbZnO_3$. *Inorg. Chem.* **2015**, *54*, 11405−11410.
(21) Li, M.-R.; Stephens, P. W.; Retuerto, M.; Sarkar, T.; Grams, C. P.; Hemberger, J.; Croft, M. C.; Walker, D.; Greenblatt, M. Designing Polar and Magnetic Oxides: Zn_2FeTaO_6 - in Search of Multiferroics. *J. Am. Chem. Soc.* **2014**, *136*, 8508−8511.
(22) Fujita, K.; Kawamoto, T.; Yamada, I.; Hernandez, O.; Hayashi, N.; Akamatsu, H.; Lafargue-Dit-Hauret, W.; Rocquefelte, X.; Fukuzumi, M.; Manuel, P.; Studer, A. J.; Knee, C. S.; Tanaka, K. $LiNbO_3$-Type $InFeO_3$: Room-Temperature Polar Magnet without Second-Order Jahn-Teller Active Ions. *Chem. Mater.* **2016**, *28*, 6644−6655.
(23) Katsumata, T.; Ohba, C.; Tobe, A.; Takeda, A.; Shoji, M.; Aimi, A.; Mori, D.; Inaguma, Y. Synthesis of New $LiNbO_3$-type Oxynitrides, $Mn(Mn_{1/6}Ta_{5/6})O_{2.5}N_{0.5}$ under High Pressure and at High Temperature. *Chem. Lett.* **2018**, *47*, 37−39.
(24) Li, Z.; Cho, Y.; Li, X.; Li, X.; Aimi, A.; Inaguma, Y.; Alonso, J. A.; Fernandez-Diaz, M. T.; Yan, J.; Downer, M. C.; Henkelman, G.; Goodenough, J. B.; Zhou, J. New Mechanism for Ferroelectricity in the Perovskite $Ca_{2-x}Mn_xTi_2O_6$ Synthesized by Spark Plasma Sinteringr. *J. Am. Chem. Soc.* **2018**, *140*, 2214−2220.
(25) Aimi, A.; Mori, D.; Hiraki, K.-i.; Takahashi, T.; Shan, Y. J.; Shirako, Y.; Zhou, J.; Inaguma, Y. High-Pressure Synthesis of A-Site Ordered Double Perovskite $CaMnTi_2O_6$ and Ferroelectricity Driven by Coupling of A-Site Ordering and the Second-Order Jahn-Teller Effect. *Chem. Mater.* **2014**, *26*, 2601−2608.
(26) Gou, G.; Charles, N.; Shi, J.; Rondinelli, J. M. A-Site Ordered Double Perovskite $CaMnTi_2O_6$ as a Multifunctional Piezoelectric and Ferroelectric-Photovoltaic Material. *Inorg. Chem.* **2017**, *56*, 11854−11861.
(27) Ruiz-Fuertes, J.; Bernert, T.; Zimmer, D.; Schrodt, N.; Koch-Müller, M.; Winkler, B.; Bayarjargal, L.; Popescu, C.; MacLeod, S.; Glazyrin, K. Ambient-temperature high-pressure-induced ferroelectric phase transition in $CaMnTi_2O_6$. *Phys. Rev. B* **2017**, *96*, 094101.
(28) Shannon, R. D. Revised effective ionic radii and systematic studies of interatomic distances in halides and chalcogenides. *Acta Crystallogr. A* **1976**, *32*, 751−767.
(29) Mo, S.; Kurauchi, Y.; Katayama, T.; Hirose, Y.; Hasegawa, T. Theoretical Investigation of the Role of the Nitride Ion in the Magnetism of Oxynitride $MnTaO_2N$. *J. Phys. Chem. C* **2019**, *123*, 25379−25384.
(30) Grins, J.; Tyutyunnik, A. Structure and Magnetic Susceptibility of $Mn_{11}Ta_4O_{21}$ and Refinement of the $Mn_4Ta_2O_9$ Structure. *J. Solid State Chem.* **1998**, *137*, 276−282.
(31) Savage, A. Pyroelectricity and Spontaneous Polarization in $LiNbO_3$. *J. Appl. Phys.* **1966**, *37*, 3071−3072.
(32) Walker, D.; Carpenter, M. A.; Hitch, C. M. Some simplifications to multianvil devices for high pressure experiments. *Am. Mineral.* **1990**, *75*, 1020−1028.
(33) Yang, T. Y.; Wen, W.; Yin, G. Z.; Li, X. L.; Gao, M.; Gu, Y. L.; Li, L.; Liu, Y.; Lin, H.; Zhang, X. M.; Zhao, B.; Liu, T. K.; Yang, Y. G.; Li, Z.; Zhou, X. T.; Gao, X. Y. Introduction of the X-ray diffraction beamline of SSRF. *Nucl. Sci. Tech.* **2015**, *26*, 20101−020101.
(34) Gao, M.; Gu, Y.; Li, L.; Gong, Z.; Gao, X.; Wen, W. Facile usage of a MYTHEN 1K with a Huber 5021 diffractometer and angular calibration in operando experiments. *J. Appl. Crystallogr.* **2016**, *49*, 1182−1189.
(35) Coelho, A. A. TOPAS and TOPAS-Academic: an optimization program integrating computer algebra and crystallographic objects written in C++. *J. Appl. Crystallogr.* **2018**, *51*, 210−218.
(36) Denton, A. R.; Ashcroft, N. W. Vegard's law. *Phys. Rev. A* **1991**, *43*, 3161−3164.
(37) Brown, I. D.; Shannon, R. D. Empirical bond-strength-bond-length curves for oxides. *Acta Crystallogr. A* **1973**, *29*, 266−282.
(38) Resta, R.; Vanderbilt, D. Theory of Polarization: A Modern Approach. *Physics of Ferroelectrics*; Springer Berlin Heidelberg, 2007; Vol. *105*, pp 31−68.
(39) Chakraborty, A.; Bouzerar, R.; Kettemann, S.; Bouzerar, G. Nanoscale inhomogeneities: A new path toward high Curie temperature ferromagnetism in diluted materials. *Phys. Rev. B: Condens. Matter Mater. Phys.* **2012**, *85*, 014201.

https://dx.doi.org/10.1021/acs.chemmater.9b05051
Chem. Mater. 2020, 32, 1618−1626